LANGMUIR

pubs.acs.org/Langmuir Article

Smart Control for Water Droplets on Temperature and Force Dual-Responsive Slippery Surfaces

Sizhu Wu, Lin Liu, Suwan Zhu,* and Yi Xiao*

Cite This: *Langmuir* 2021, 37, 578−584 Read Online

ACCESS | Metrics & More | Article Recommendations | Supporting Information

ABSTRACT: Responsive slippery lubricant-infused porous surfaces (SLIPSs), featuring excellent liquid repelling/sliding capabilities in response to external stimuli, have attracted great attention in smart droplet manipulations. However, most of the reported responsive SLIPSs function under a single stimulus. Here, we report a kind of smart slippery surface capable of on-demand control between sliding and pinning for water droplets via alternately freezing/thawing the stretchable polydimethylsiloxane sheet in different strains. Diverse parameters are quantified to investigate the critical sliding volume of the droplet, including lubricant infusion amount, laser-scanning power, and pillar spacing. By virtue of the cooperation of temperature and force fields acting on the SLIPS, we demonstrate the intriguing applications including controllable chemical reaction and on-demand electrical circuit control. We envision that this dual-responsive surface should provide more possibilities in smart control of microscale droplets, especially in active vaccine-involved biochemical microreactions where a lower temperature is highly favored.

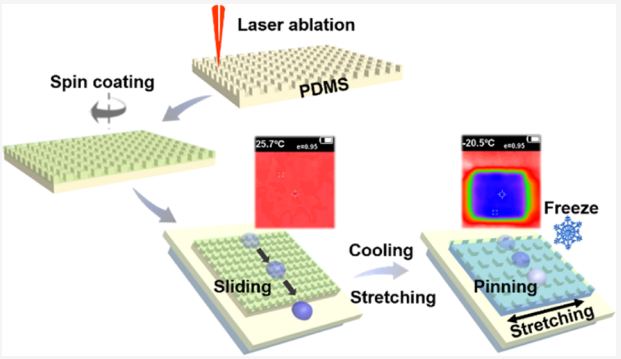

INTRODUCTION

Liquid droplet manipulations, such as droplet storage, transfer, and mixing, have garnered widespread attention because of their potential applications in cell screening, biochemical synthesis, and molecular sensing.[1−4] Generally, most functional surfaces for droplet manipulations can be categorized into superhydrophobic surfaces[5,6] and slippery lubricant-infused porous surfaces (SLIPSs) based on the special interaction among multiple phases.[7,8] As an emerging functional surface inspired by the Nepenthes pitcher plant, SLIPS shows excellent nonselective liquid repellency and a low hysteresis feature (<5°) and has attracted considerable interest in the field of interfacial science and related applications such as drag reduction, antifouling, anti-icing, and bubble and droplet manipulation.[9−13] For instance, Cao et al. demonstrate that the orthogonal assembly of anisotropic tracks can realize unidirectional droplet manipulation by fusing the bioinspirations of the rice leaf and the pitcher plant.[13] Levkin et al. construct patterned slippery surfaces for precisely positioning and guiding the droplets up to volumes of several microliters.[14] Usually, these approaches can be classified into the same category that relies on the assistance of Laplace pressure arising from the asymmetry of droplet shape caused by the substrate's morphology.

In the past years, smart surfaces with switchable wettability have been proposed and extensively studied in both academic research and industrial applications, such as oil−water separation, droplet transportation, cell capture/release, and biotechnology.[15−18] By virtue of diverse external stimuli including photoirradiation, temperature, magnetic field, pH, and others,[19−22] switchable droplet manipulation can be achieved by the regulation of the chemical composition and geographic morphology on the smart surfaces. Typically, Wang et al. achieved programmable wettability by utilizing paraffin-infused porous graphene films through dynamic and reversible transition on liquid/solid surfaces in response to near-infrared light.[23] Wu et al. fabricated a kind of Fe_3O_4-doped SLIPS, which can easily manipulate diverse liquids in arbitrary directions by a unilateral near-infrared-irradiation stimulus.[24] Nevertheless, most of the reported stimuli-responsive SLIPSs work under single-stimulus conditions, which greatly hinder their widespread uses. Although dual-responsive SLIPSs (e.g., photoelectric synergetic responsive polymers) have been reported for droplet manipulations in previous studies, the targeted liquids are usually limited to specific properties (e.g., electroconductivity).[25,26] Hence, it is interesting to develop more flexible multiresponsive SLIPSs.

Herein, we propose and fabricate a kind of dual-responsive smart SLIPS (DRSS) by femtosecond laser cross-scanning on flexible polydimethylsiloxane (PDMS) sheets. By cooperation of alternately freezing/thawing and stretching the DRSS, the

Received: November 17, 2020
Revised: December 15, 2020
Published: December 28, 2020

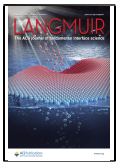

https://dx.doi.org/10.1021/acs.langmuir.0c03308
Langmuir 2021, 37, 578−584

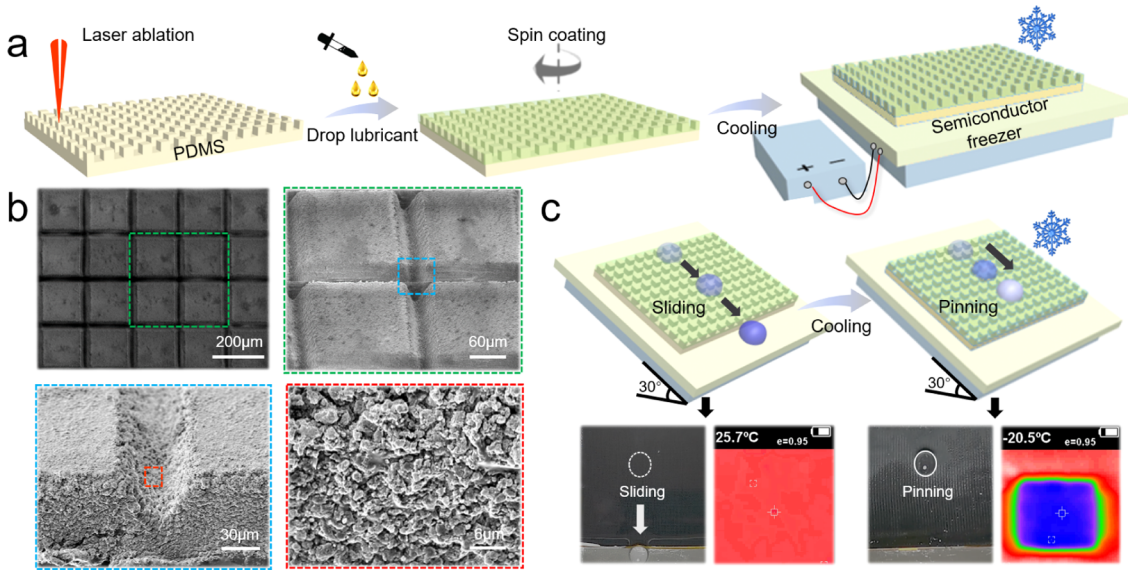

Figure 1. Schematic fabrication of the DRSS and its droplet control. (a) The DRSS is constructed through femtosecond laser cross-scanning and filling lubricating oil on PDMS. (b) SEM images of the micropillar structures on the DRSS at different magnifications. (c) An 8 μL water droplet can readily slide off along the DRSS at room temperature but sticks onto the surface when the temperature is decreased to −20.5 °C (tilt angle = 30°).

controllable behavior between sliding and pinning for various microsized droplets is achieved. The critical sliding volume of the droplet is investigated under diverse experimental parameters, including lubricant infusion amount, laser-scanning power, and pillar spacing. The underlying mechanism is discussed and is attributed to the friction resistance regulation at the DRSS−droplet interface induced by both stretching force and temperature fields, which change the surface roughness and the targeted droplet physical state on the DRSS. Based on the selective volume screening function between droplet sliding and pinning, we demonstrate the intriguing applications including microsized microfluidic reactors and electric circuit on/off control. This work should provide new insight into smart manipulation of microscale droplets in practical scenarios such as active biochemical microreactions at a lower temperature.

EXPERIMENTAL SECTION

Materials and Fabrication. Commercially available black PDMS sheets (thickness ~200 μm) were cut into appropriate sizes. Thereafter, the PDMS sheets were mounted on an $x-y-z$ mobile platform and ablated via cross-scanning femtosecond laser scanning at a speed 2 mm/s to form micropillar structures on PDMS sheets. The scanning spacing between two adjacent lines was 200 μm in both x- and y- coordinate directions. The laser pulses (a central wavelength of 800 nm, a repetition rate of 1 kHz) from a regenerative amplified Ti:sapphire femtosecond laser system (Coherent Physics, USA) were employed for ablation. The laser beam was guided onto the PDMS substrate surface through a galvanometric scanning system (SCANLAB, Germany), which was equipped with a 63 mm telecentric $f-\theta$ lens to make the laser beam focus and scan along the x/y coordinate direction. The laser-induced microstructured surface needed to be spun with silicone oil. The adjustable rotation speed of the spin coater was between 100 and 7000 rpm at factory settings. The typical rotational speed in our sample preparation was ~350 rpm, and the rotational time ranged from 1 to 5 min.

Observation of the Oil Film Thickness. To calculate the oil film thickness of the DRSS, we first put the DRSS on the microscope worktable. The iron powder with a diameter of 5 μm was coated onto the top of the oil film. Second, the first value was recorded when the microscope was focused on the top of the micropillar of dry microstructured PDMS, and the second value was recorded when the microscope was focused on the iron particles. Finally, we calculated the difference between the two values, which represented the thickness of the oil film. The minimum resolution of the microscope is 2 μm. Consequently, the thickness of the oil film is calculated to be ~40 μm.

Characterization. Scanning electron microscopy (SEM) photos were utilized to analyze the surface topography of the laser-induced PDMS substrate via use of a field emission scanning electron microscope (JEOL, Japan).

Water Droplet Sliding/Pinning Strategy. After spin-coating processing, the oil-infused microstructured surface was placed on a homemade semiconductor freezer. The DRSS will be capable of on-demand control between sliding and pinning for water droplets via alternately freezing/thawing the stretchable PDMS sheet in different strains.

RESULTS AND DISCUSSION

The DRSS fabrication process consists of two steps. First, the commercially available PDMS sheet (~200 μm thickness) was converted via femtosecond laser cross-scanning irradiation into a superhydrophobic micropillar-arrayed PDMS, which was frequently adopted in recent functional surface fabrication.[27,28] Second, the as-prepared sample was then impregnated by silicone oil (50 cSt viscosity) through spin coating, resulting in an oil film formation on the surface (Figure 1a). SEM images in Figure 1b show the surface morphology of the laser-induced micropillar structures on PDMS at different magnifications. Because of the interaction between the laser pulse and PDMS, nanoparticles were randomly generated on the surface after laser ablation. To achieve the selective motion between sliding and pinning for the water droplet, we adopted a dual-control strategy by alternately freezing/thawing and stretching the DRSS. As a typical demonstration, Figure 1c shows that an 8 μL water droplet could readily slide off the DRSS (a tilt angle of 30°) at room temperature (25 °C). However, the water droplet froze and stuck on the inclined DRSS as the temperature was decreased to −20.5 °C utilizing a homemade semiconductor freezer.

To elucidate the basic physics behind the sliding/pinning motion of droplets on the DRSS (Figure 1c), we gave out the force analysis for a sliding droplet on the DRSS. When a droplet

https://dx.doi.org/10.1021/acs.langmuir.0c03308
Langmuir 2021, 37, 578−584

slides off along the DRSS at room temperature (Figure 2a), there are generally three forces acting on the droplet, which are the gravitational force G, the support force F_s, and the total frictional force F_f. Note that the support force F_s and the vertical-direction component of the gravitational force $mg\cos\alpha$ from the opposite directions cancel out. The driving force of droplet motion is the axis-direction component of gravity, which is calculated as

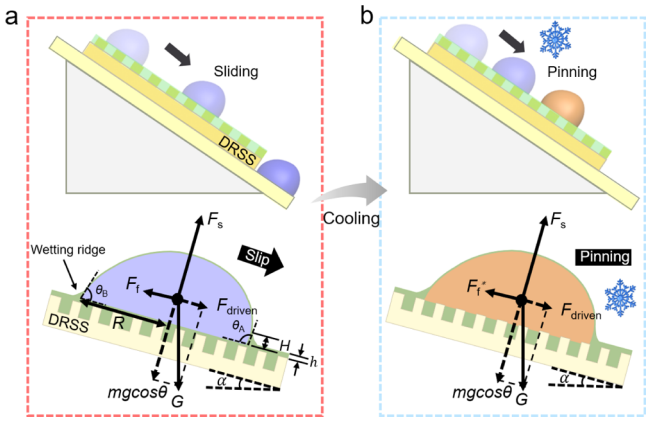

Figure 2. Schematics and force analysis of droplet sliding and pinning behaviors on the DRSS at (a) room temperature and (b) low temperature. Once the droplet freezes, the liquid–liquid interface between the droplet and DRSS will convert into the solid–liquid interface. At this point, the movement friction is dominated by the contact line friction, and the interfacial friction is negligible.

$$F_{\text{driven}} = mg\sin\alpha = \rho_D \Omega g \sin\alpha \quad (1)$$

where α is the inclined angle, m and g correspond to the mass of the droplet and the acceleration due to gravity, respectively, Ω is the droplet volume, and ρ_D represents the density of the droplet. The total motion resistance is composed of the contact angle hysteresis (CAH) of the droplet and the drag force (viscous and pinning). The resistance of CAH can be calculated as[29]

$$F_{\text{CAH}} = \gamma L(\cos\theta_B - \cos\theta_A) \quad (2)$$

where γ is the surface tension of media, L is the droplet's character length, and θ_A and θ_B are the advancing and receding angles of the droplet, respectively. The droplet on SLIPS generally shows an extremely low CAH and excellent liquid repellency.[7,30] Hence, F_{CAH} can be negligible.[7]

In addition, the droplet motion is also affected by different kinds of dissipations between two liquids including the droplet and lubricating oil. The scale of viscous stress on the droplet and oil sides at an oil–water interface can be written as $\mu_D(V - V_i)/R$ and $\mu_O V_i/h$, where μ_D is the viscosity of the droplet, μ_O is the viscosity of the oil, R is the droplet base radius, h is the lubricating film thickness, V is the droplet slip velocity, and V_i is the velocity of the oil–water interface.[31] In equilibrium, balancing the viscous stress on either side of the interface provides $\mu_D(V - V_i)/R = \mu_O V_i/h$ and $V_i = V(1 + \mu_O R/\mu_D h)^{-1}$.[32] In our experiment, $\mu_D \ll \mu_O$, and the above scaling relation can be reduced to $V_i \approx V\mu_D h/\mu_O R$. When it integrates over a surface area of order R^2, we get the viscous stress in a droplet which scales as $\mu_D V/R$, which demonstrates that the dissipation in the droplet is due to the change in the droplet base radius induced

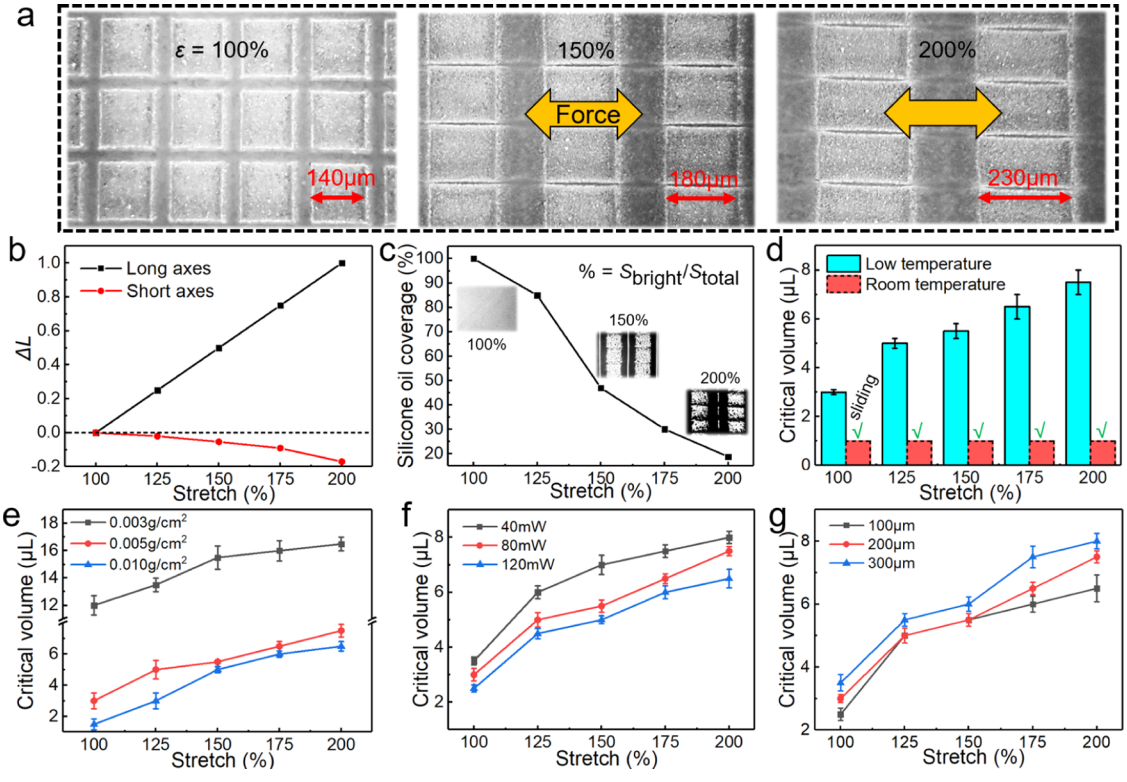

Figure 3. DRSS response to different stretching ratios (ε from 100 to 200%) and temperature fields. (a) Optical morphologies of a laser-ablated PDMS sheet. (b) DRSS lengths of the long axis and short axis. (c) Silicone oil coverage on the DRSS (inset: optical images of the DRSS). (d) Comparison of critical sliding volume between room temperature and low temperature (tilt angle = 45°, blue column: −20.5 °C, red column: 25 °C). Critical sliding volume for sliding/pinning behavior of the droplet on the stretchable DRSS in diverse experimental parameters including (e) lubricant infusion amount, (f) laser-scanning power, and (g) pillar spacing.

https://dx.doi.org/10.1021/acs.langmuir.0c03308
Langmuir 2021, 37, 578−584

by the change of the surface tension of the droplet. The viscous force in the droplet (F_D) scales as[33]

$$F_D \approx \mu_D VR \tag{3}$$

As a droplet on an oil-coated surface is surrounded by a wetting ridge made of oil, viscous dissipation in the oil takes place in the oil film underneath the droplet and wetting ridge. The viscous stress underneath the oil film scales as $\mu_O V_i/h$, which after integration gives the viscous force (F_U) as $\mu_O V_i R^2/h$. In our experiment, $\mu_D \ll \mu_O$, and it can further be simplified to[33]

$$F_U \approx \mu_D VR \tag{4}$$

The viscous stress in the wetting ridge of height H scales as $\mu_O V/H$. Integrating it over a surface area of HR results in the Stokes force (F_R) as[31,32]

$$F_R \approx \mu_O VR \tag{5}$$

Therefore, the total frictional force is the sum of all the dissipative forces and the pinning force[33]

$$F_f = F_D + F_U + F_R + F_P \tag{6}$$

where $F_P = \rho\Omega g \sin\alpha^*$ is the pinning force[31] and α^* is the critical inclined angle.

The alternating temperature field is critical to droplet sliding/pinning control. Specifically, when a low-temperature field is applied on the DRSS (Figure 2b), the interfacial friction increases according to above-mentioned analysis, subsequently slowing down the downward momentum of the sliding droplet. The residence time between the droplet and the DRSS will be subsequently prolonged, followed by the increase of heat exchange on the interface. Once the bottom of the droplet freezes, the liquid−liquid interface between the droplet and DRSS converts into the solid−liquid interface. At this point, the droplet movement friction is dominated by the contact line friction, and the interfacial friction only plays a minor role. In contrast, the contact line friction on SLIPS is negligible at the liquid−liquid interfaces.[34] Daniel et al.[35] demonstrate that there is no three-phase contact line for a moving droplet on a lubricated surface, and the film thickness follows the Landau−Levich−Derjaguin law

$$h \sim RCa^{2/3} \tag{7}$$

where capillary number $Ca = \mu_O V_i/\gamma$ and γ is the water−oil interfacial tension. The droplet is therefore oleoplaning with a minimal dissipative force and no contact line pinning.[31] That is to say, at a lower temperature, the contact line friction of a frozen droplet introduces the significant increase in systematic dissipation, which subsequently results in the pinning effect of the droplet sliding on the cold DRSS.

Moreover, by adjusting different bidirectional forces on the DRSS, the surface roughness can be reversibly modified. Figure 3a shows the optical morphologies of a laser-ablated PDMS sheet in different stretching ratios (ε = 100, 150, and 200%) after one-direction mechanical stretching. The stretching ratio is defined as $\varepsilon = L/L_0$, where L and L_0 denote the length of the processing area in the stretching state and in the pristine state, respectively. It can be clearly seen that the PDMS length of the long axis (along the stretching direction) after stretching increased almost linearly with the elevated strain, while the short axis (perpendicular to the stretching direction) decreased slightly (Figure 3b). In addition, the silicone oil coverage on the DRSS was found to decrease with the increased stretching ratio (Figures 3c and S1). It can be observed that the oil surface on the pristine DRSS shows uniform brightness. Once the stretching force was applied, the unbroken bright area was fragmentized with the emergent of the dark area (the underneath PDMS). We accordingly used an image processing approach to calculate the oil coverage area by the ratio of the extracted bright pixels and dark pixels. At the pristine state (ε = 100%), the silicone oil completely covered the microstructure (bright area). With the increase of the stretching ratio, the oil film became thinner (dark area) and the surface roughness increased because of the appearance of the micropillar structures. Specifically, the stretching ratio ε = 150% suggests that the surface oil coverage approximately decreased by half. While the stretching ratio increased to 200%, the surface oil proportion dropped to ∼15%. Note that a thinner oil film may lead to the contact between droplets and micropillars, which in turn enhances the surface roughness and interfacial friction between the droplet and DRSS.

In general, the reversible control between sliding and pinning for droplets on SLIPS is one of the most important metrics considered in SLIPS designs. Therefore, the effect of both temperature and force on the DRSS has been investigated in detail. We first focused on the temperature regulation on the critical sliding volume (i.e., the minimum volume for the droplet that slides on an inclined DRSS), as shown in Figure 3d (tilt angle = 45°, blue column: −20.5 °C, red column: 25 °C). The DRSS was set at a typical inclined angle of 45°, and the water droplet volumes ranged from 1 to 20 μL. At room temperature, a minimum droplet of 1 μL was found to easily slide off the DRSS at different stretching ratios ranging from 100 to 200% (red column). When under low-temperature conditions, this threshold increased significantly from 3 to 7.5 μL versus 100 to 200% in stretching ratio (blue column).

We next investigated the critical sliding volume on the DRSS in different stretching ratios from 100 to 200% at low temperature. We consider the following experimental parameters: lubricant infusion amount, laser-scanning power, and pillar spacing. The low-temperature condition was created and kept at −21 ± 1 °C using a homemade semiconductor freezer setup below the DRSS. Figure 3e shows the influence of lubricant infusion amounts (0.003, 0.005, and 0.01 g/cm^2) on the critical sliding volume with different stretching ratios, where lubricant infusion amount is defined as the ratio between the infused silicone oil mass and the processing area. The critical sliding volume exhibits an obvious difference: with the increase of the lubricant infusion amount, the critical sliding volume decreased for each stretching ratio. Taking 0.005 g/cm^2 as an example (red line), the critical sliding volume increased with an elevated stretching ratio. Particularly, the critical sliding volume was 3 μL for pristine sample and increased to 7 μL, while the maximum stretching ratio was 200%. Figure 3f shows the influence of different laser-scanning powers (40, 80, and 120 mW) on droplet sliding behavior. Note that larger laser ablation energy would result in wider and deeper grooves (Figure S2), leading to enhanced oil storage capacities. Accordingly, when the laser-scanning power increased, the critical sliding volume decreased for the same stretching ratio. Figure 3g shows the influence of the pillar spacings (100, 200, and 300 μm) on the critical sliding volume. When the pillar spacing increased, the threshold corresponding to each stretching ratio slightly decreased.

The threshold generally exhibited a significant uptrend as the stretching ratio was elevated in Figure 3e−g, which demonstrated the effective mechanical response of the DRSS in droplet control. The increase of the stretching ratio will lead to the

https://dx.doi.org/10.1021/acs.langmuir.0c03308
Langmuir 2021, 37, 578−584

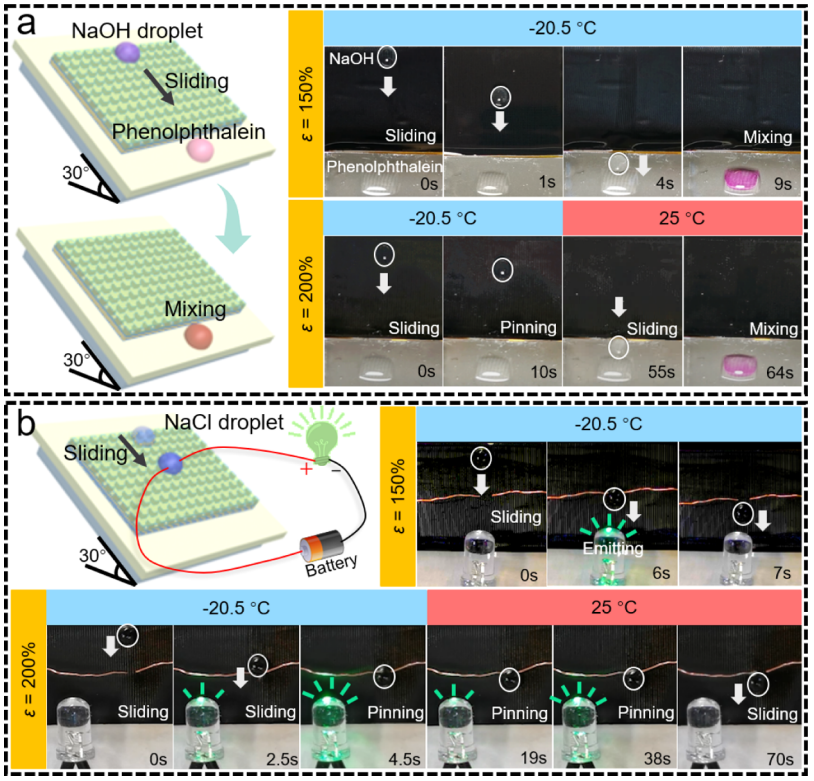

Figure 4. Demonstrations for the microsized microfluidic reactor and electric circuit on/off control on the DRSS (tilt angle = 30°). (a) Controllable coalescence between the NaOH droplet and phenolphthalein. (b) On-demand light control of the electric circuit using a saturated NaCl droplet in an alternating temperature field.

decrease of the oil film thickness (Figure 3c). Our result exhibits good consistency with previous study.[33] This is mainly due to the fact that the introduction of an oil layer covers the defects and pinning sites of the solid surface and provides a lubricated surface, which triggers smooth contact line motion for slipping drops. Once the stretching ratio increases, the lubricant thickness will decrease; hence, the slip velocity of the droplet subsequently decreases as the surface becomes less lubricated with increased pinning effect. It should be emphasized that the stretching force can also achieve in situ sliding/pinning control for the droplet during its downward sliding motion (Figure S3 and Movie S1). Besides, we observed that the environmental water vapor in a wide range (the relative humidity, RH, varies from 34 to 90%) has no significant impact on the droplet sliding behaviors on the DRSS (Figure S4 and Movie S2).

Hence, by the cooperation of mechanically stretching and alternately freezing/thawing the DRSS, we have shown the capability of on-demand sliding/pinning control for various microsized droplets for the DRSS. Compared with those reported approaches to droplet sliding/pinning control that solely rely on mechanical stretching,[36,37] we unlock an alternative option (temperature field) for the flexible droplet manipulations. Moreover, different from most thermoresponsive surfaces working at high temperatures (dozens of degrees or even higher) beyond the solid lubricant melting point, which may cause the macroscopic evaporation of the microsized droplet and chemical pollution from the heated lubricant,[38−40] our DRSS functions at a much lower temperature and features the distinct advantages of low pollution and low liquid evaporation loss during the droplet manipulation process.

The potential applications for multiresponsive slippery surfaces can also be expanded to biomedical, microfluidic, and other related fields.[25] Finally, based on the selective screening in droplet volumes on the DRSS, we demonstrate several intriguing applications including microsized microfluidic reactors and electric circuit on/off control. Figure 4a exhibits the color rendering chemical reaction between NaOH and phenolphthalein droplets (Movie S3). A transparent NaOH droplet (8 μL) could readily slide off along the cold DRSS (−20.5 °C, a tilt angle of 30°) and reacted with phenolphthalein at a stretching ratio of 150% at time t = 9 s. When the stretching ratio increased to ε = 200%, the NaOH droplet only slid down a short distance on the cold DRSS and then froze on the surface. Once the surface temperature was elevated (25 °C), the droplet could continue to slide downward and mixed with phenolphthalein at time t = 64 s. Note that the freezing at the bottom side of a droplet is the function of temperature and stay time. Consequently, at a stretching ratio of 150%, the droplet mobility is relatively fast, so the droplet does not have enough time to be frozen even at −20.5 °C. When the stretching ratio is increased to 200%, the droplet mobility is slowed down, where it can have enough time to be frozen at −20.5 °C (Movie S3). The on-demand control of a light-emitting diode (LED) light is also shown in Figure 4b (Movie S4). A saturated NaCl droplet (8 μL) slid initially downward along the cold DRSS (tilt angle = 30° and ε = 150%). The LED could light up as the droplet passed through the copper wire and then extinguished as it slid away. When the stretching ratio increased at ε = 200%, the NaCl droplet pinned at the wire joint, bridging the gap between the power source and the LED with light on. Once the substrate temperature was elevated, the droplet melted and slid away, followed by the extinguishment of the LED light.

https://dx.doi.org/10.1021/acs.langmuir.0c03308
Langmuir 2021, 37, 578−584

CONCLUSIONS

In conclusion, a kind of DRSS was proposed and fabricated by femtosecond laser cross-scanning on flexible PDMS sheets, followed by the simple infusion of silicone oil into the microstructures. This DRSS is capable of in situ manipulating microsized droplet motion between sliding and pinning under dual stimuli of freezing/thawing and bidirectional stretching. By changing experimental conditions such as lubricant infusion amount, laser-scanning power, and pillar spacing, one can readily achieve the switchable sliding/pinning control of droplets in different volumes. The basic mechanism is attributed to the friction resistance regulation at the DRSS−droplet interface induced by both force and temperature fields. Based on the powerful DRSS, we also demonstrate the intriguing applications such as microscale chemical reactions and electric circuit on/off control. This dual-responsive SLIPS should open up more possibilities in controllable droplet manipulation and smart surface designs, especially in active biochemical engineering where a lower temperature is usually needed.

ASSOCIATED CONTENT

Supporting Information

The Supporting Information is available free of charge at https://pubs.acs.org/doi/10.1021/acs.langmuir.0c03308.

In situ control of the droplet by stretching force (MP4)

Influence of relative humidity on the droplet motion behaviors (MP4)

Controllable coalescence between the NaOH droplet and phenolphthalein (MP4)

On-demand on/off control of the LED light (MP4)

Comparison of the optical images of the DRSS sheet before and after force stretching; SEM images showing groove depth with different laser-scanning powers; in situ control of droplet by stretching force; influence of different relative humidities on the droplet motion behaviors (PDF)

AUTHOR INFORMATION

Corresponding Authors

Suwan Zhu − *CAS Key Laboratory of Mechanical Behavior and Design of Materials, Department of Precision Machinery and Precision Instrumentation, University of Science and Technology of China, Hefei 230026, China;* orcid.org/0000-0001-9881-5694; Email: suwanzhu@ustc.edu.cn

Yi Xiao − *School of Mechanical Engineering, Nantong Vocational University, Nantong 226007, China;* Email: xiaoyiphd@163.com

Authors

Sizhu Wu − *School of Instrument Science and Opto-Electronics Engineering and Intelligent Interconnected Systems Laboratory of Anhui Province, Hefei University of Technology, Hefei 230009, China*

Lin Liu − *School of Instrument Science and Opto-Electronics Engineering, Hefei University of Technology, Hefei 230009, China*

Complete contact information is available at: https://pubs.acs.org/10.1021/acs.langmuir.0c03308

Notes

The authors declare no competing financial interest.

ACKNOWLEDGMENTS

This work was supported by the National Natural Science Foundation of China (no. 51875160), the Fundamental Research Funds for the Central Universities (nos. PA2020GDKC0010 and WK2480000005), the Natural Science Foundation of Jiangsu Province (no. BK20191209), the Qing Lan Project of the Jiangsu Province Higher Education Institutions of China (2019), and the 226 High-level Talents Training Project of Nantong (no. 2018-01). The authors acknowledge the Experimental Center of Engineering and Materials Sciences at USTC for the fabrication and measurement of samples.

REFERENCES

(1) Ueda, E.; Geyer, F. L.; Nedashkivska, V.; Levkin, P. A. DropletMicroarray: facile formation of arrays of microdroplets and hydrogel micropads for cell screening applications. *Lab Chip* **2012**, *12*, 5218−5224.

(2) Popova, A. A.; Demir, K.; Hartanto, T. G.; Schmitt, E.; Levkin, P. A. Droplet-microarray on superhydrophobic−superhydrophilic patterns for high-throughput live cell screenings. *RSC Adv.* **2016**, *6*, 38263−38276.

(3) Minemawari, H.; Yamada, T.; Matsui, H.; Tsutsumi, J. Y.; Haas, S.; Chiba, R.; Kumai, R.; Hasegawa, T. Inkjet printing of single-crystal films. *Nature* **2011**, *475*, 364−367.

(4) Xu, L.-P.; Chen, Y.; Yang, G.; Shi, W.; Dai, B.; Li, G.; Cao, Y.; Wen, Y.; Zhang, X.; Wang, S. Ultratrace DNA Detection Based on the Condensing-Enrichment Effect of Superwettable Microchips. *Adv. Mater.* **2015**, *27*, 6878−6884.

(5) Jokinen, V.; Sainiemi, L.; Franssila, S. Complex droplets on chemically modified silicon nanograss. *Adv. Mater.* **2008**, *20*, 3453−3456.

(6) Wu, D.; Wu, S.-Z.; Chen, Q.-D.; Zhang, Y.-L.; Yao, J.; Yao, X.; Niu, L.-G.; Wang, J.-N.; Jiang, L.; Sun, H.-B. Curvature-Driven Reversible In Situ Switching Between Pinned and Roll-Down Superhydrophobic States for Water Droplet Transportation. *Adv. Mater.* **2011**, *23*, 545−549.

(7) Wong, T.-S.; Kang, S. H.; Tang, S. K. Y.; Smythe, E. J.; Hatton, B. D.; Grinthal, A.; Aizenberg, J. Bioinspired self-repairing slippery surfaces with pressure-stable omniphobicity. *Nature* **2011**, *477*, 443−447.

(8) Guo, T.; Che, P.; Heng, L.; Fan, L.; Jiang, L. Anisotropic Slippery Surfaces: Electric-Driven Smart Control of a Drop's Slide. *Adv. Mater.* **2016**, *28*, 6999−7007.

(9) Wang, Y.; Zhang, H.; Liu, X.; Zhou, Z. Slippery liquid-infused substrates: a versatile preparation, unique anti-wetting and drag-reduction effect on water. *J. Mater. Chem. A* **2016**, *4*, 2524−2529.

(10) Sunny, S.; Vogel, N.; Howell, C.; Vu, T. L.; Aizenberg, J. Lubricant-Infused Nanoparticulate Coatings Assembled by Layer-by-Layer Deposition. *Adv. Funct. Mater.* **2014**, *24*, 6658−6667.

(11) Juuti, P.; Haapanen, J.; Stenroos, C.; Niemelä-Anttonen, H.; Harra, J.; Koivuluoto, H.; Teisala, H.; Lahti, J.; Tuominen, M.; Kuusipalo, J.; Vuoristo, P.; Mäkelä, J. M. Achieving a slippery, liquid-infused porous surface with anti-icing properties by direct deposition of flame synthesized aerosol nanoparticles on a thermally fragile substrate. *Appl. Phys. Lett.* **2017**, *110*, 161603.

(12) Lv, X.; Jiao, Y.; Wu, S.; Li, C.; Zhang, Y.; Li, J.; Hu, Y.; Wu, D. Anisotropic Sliding of Underwater Bubbles On Microgrooved Slippery Surfaces by One-Step Femtosecond Laser Scanning. *ACS Appl. Mater. Interfaces* **2019**, *11*, 20574−20580.

(13) Li, P.; Cao, M.; Bai, H.; Zhao, T.; Ning, Y.; Wang, X.; Liu, K.; Jiang, L. Unidirectional Liquid Manipulation Via an Integrated Mesh with Orthogonal Anisotropic Slippery Tracks. *Adv. Funct. Mater.* **2019**, *29*, 1904446.

(14) Paulssen, D.; Hardt, S.; Levkin, P. A. Droplet Sorting and Manipulation on Patterned Two-Phase Slippery Lubricant-Infused Surface. *ACS Appl. Mater. Interfaces* **2019**, *11*, 16130−16138.

(15) Su, X.; Li, H.; Lai, X.; Zhang, L.; Liao, X.; Wang, J.; Chen, Z.; He, J.; Zeng, X. Dual-Functional Superhydrophobic Textiles with Asymmetric Roll-Down/Pinned States for Water Droplet Transportation and Oil-Water Separation. *ACS Appl. Mater. Interfaces* **2018**, *10*, 4213−4221.
(16) Tang, X.; Wang, L. Loss-Free Photo-Manipulation of Droplets by Pyroelectro-Trapping on Superhydrophobic Surfaces. *ACS Nano* **2018**, *12*, 8994−9004.
(17) Lourenço, B. N.; Marchioli, G.; Song, W.; Reis, R. L.; Van Blitterswijk, C. A.; Karperien, M.; Van Apeldoorn, A.; Mano, J. F. Wettability Influences Cell Behavior on Superhydrophobic Surfaces with Different Topographies. *Biointerphases* **2012**, *7*, 46.
(18) Wang, L.; Wang, H.; Yuan, L.; Yang, W.; Wu, Z.; Chen, H. Stepwise control of protein adsorption and bacterial attachment on a nanowire array surface: tuning surface wettability by salt concentration. *J. Mater. Chem.* **2011**, *21*, 13920−13925.
(19) Pan, S.; Guo, R.; Xu, W. Photoresponsive superhydrophobic surfaces for effective wetting control. *Soft Matter* **2014**, *10*, 9187−9192.
(20) Gao, C.; Wang, L.; Lin, Y.; Li, J.; Liu, Y.; Li, X.; Feng, S.; Zheng, Y. Droplets Manipulated on Photothermal Organogel Surfaces. *Adv. Funct. Mater.* **2018**, *28*, 1803072.
(21) Cao, M.; Jin, X.; Peng, Y.; Yu, C.; Li, K.; Liu, K.; Jiang, L. Unidirectional Wetting Properties on Multi-Bioinspired Magneto-controllable Slippery Microcilia. *Adv. Mater.* **2017**, *29*, 1606869.
(22) Xu, Z.; Zhao, Y.; Wang, H.; Zhou, H.; Qin, C.; Wang, X.; Lin, T. Fluorine-Free Superhydrophobic Coatings with pH-induced Wettability Transition for Controllable Oil-Water Separation. *ACS Appl. Mater. Interfaces* **2016**, *8*, 5661−5667.
(23) Wang, J.; Gao, W.; Zhang, H.; Zou, M. H.; Chen, Y. P.; Zhao, Y. J. Programmable wettability on photocontrolled graphene film. *Sci. Adv.* **2018**, *4*, No. eaat7392.
(24) Wu, S.; Zhou, L.; Chen, C.; Shi, L.-A.; Zhu, S.; Zhang, C.; Meng, D.; Huang, Z.; Li, J.; Hu, Y.; Wu, D. Photothermal Actuation of Diverse Liquids on an Fe_3O_4-Doped Slippery Surface for Electric Switching and Cell Culture. *Langmuir* **2019**, *35*, 13915−13922.
(25) Wang, Z.; Liu, Y.; Guo, P.; Heng, L.; Jiang, L. Photoelectric Synergetic Responsive Slippery Surfaces Based on Tailored Anisotropic Films Generated by Interfacial Directional Freezing. *Adv. Funct. Mater.* **2018**, *28*, 1801310.
(26) Han, K.; Heng, L.; Zhang, Y.; Liu, Y.; Jiang, L. Slippery Surface Based on Photoelectric Responsive Nanoporous Composites with Optimal Wettability Region for Droplets' Multifunctional Manipulation. *Adv. Sci.* **2019**, *6*, 1801231.
(27) Cheng, Y.; Yang, Q.; Fang, Y.; Yong, J.; Chen, F.; Hou, X. Underwater Anisotropic 3D Superoleophobic Tracks Applied for the Directional Movement of Oil Droplets and the Microdroplets Reaction. *Adv. Mater. Interfaces* **2019**, *6*, 1900067.
(28) Yong, J.; Bai, X.; Yang, Q.; Hou, X.; Chen, F. Filtration and removal of liquid polymers from water (polymer/water separation) by use of the underwater superpolymphobic mesh produced with a femtosecond laser. *J. Colloid Interface Sci.* **2021**, *582*, 1203−1212.
(29) Yu, C.; Zhu, X.; Li, K.; Cao, M.; Jiang, L. Manipulating Bubbles in Aqueous Environment via a Lubricant-Infused Slippery Surface. *Adv. Funct. Mater.* **2017**, *27*, 1701605.
(30) Cui, W.; Pakkanen, T. A. Fabrication of transparent icephobic surfaces with self-reparability: Effect of structuring and thickness of the lubricant-elastomer layer. *Appl. Surf. Sci.* **2020**, *504*, 144061.
(31) Smith, J. D.; Dhiman, R.; Anand, S.; Reza-Garduno, E.; Cohen, R. E.; McKinley, G. H.; Varanasi, K. K. Droplet mobility on lubricant-impregnated surfaces. *Soft Matter* **2013**, *9*, 1772−1780.
(32) Keiser, A.; Keiser, L.; Clanet, C.; Quéré, D. Drop friction on liquid-infused materials. *Soft Matter* **2017**, *13*, 6981−6987.
(33) Sharma, M.; Roy, P. K.; Barman, J.; Khare, K. Mobility of Aqueous and Binary Mixture Drops on Lubricating Fluid-Coated Slippery Surfaces. *Langmuir* **2019**, *35*, 7672−7679.
(34) Gao, N.; Geyer, F.; Pilat, D. W.; Wooh, S.; Vollmer, D.; Butt, H.-J.; Berger, R. How drops start sliding over solid surfaces. *Nat. Phys.* **2018**, *14*, 191−196.
(35) Daniel, D.; Timonen, J. V. I.; Li, R.; Velling, S. J.; Aizenberg, J. Oleoplaning droplets on lubricated surfaces. *Nat. Phys.* **2017**, *13*, 1020−1025.
(36) Wang, J.-N.; Liu, Y.-Q.; Zhang, Y.-L.; Feng, J.; Wang, H.; Yu, Y.-H.; Sun, H.-B. Wearable Superhydrophobic Elastomer Skin with Switchable Wettability. *Adv. Funct. Mater.* **2018**, *28*, 1800625.
(37) Zhang, Y.; Jiao, Y.; Chen, C.; Zhu, S.; Li, C.; Li, J.; Hu, Y.; Wu, D.; Chu, J. Reversible Tuning between Isotropic and Anisotropic Sliding by One-Direction Mechanical Stretching on Microgrooved Slippery Surfaces. *Langmuir* **2019**, *35*, 10625−10630.
(38) Chen, C.; Huang, Z.; Jiao, Y.; Shi, L.-A.; Zhang, Y.; Li, J.; Li, C.; Lv, X.; Wu, S.; Hu, Y.; Zhu, W.; Wu, D.; Chu, J.; Jiang, L. In Situ Reversible Control between Sliding and Pinning for Diverse Liquids under Ultra-Low Voltage. *ACS Nano* **2019**, *13*, 5742−5752.
(39) Gulfam, R.; Orejon, D.; Choi, C.-H.; Zhang, P. Phase-Change Slippery Liquid-Infused Porous Surfaces with Thermo-Responsive Wetting and Shedding States. *ACS Appl. Mater. Interfaces* **2020**, *12*, 34306−34316.
(40) Zhang, J.; Wu, L.; Li, B.; Li, L.; Seeger, S.; Wang, A. Evaporation-Induced Transition from Nepenthes Pitcher-Inspired Slippery Surfaces to Lotus Leaf-Inspired Superoleophobic Surfaces. *Langmuir* **2014**, *30*, 14292−14299.

https://dx.doi.org/10.1021/acs.langmuir.0c03308
Langmuir 2021, 37, 578−584